ACS Catalysis

pubs.acs.org/acscatalysis
Research Article

Kinetic Monte Carlo Analysis Reveals Non-mean-field Active Site Dynamics in Cu−Zeolite-Catalyzed NO_x Reduction

Anshuman Goswami, Siddarth H. Krishna, Rajamani Gounder, and William F. Schneider*

Cite This: ACS Catal. 2024, 14, 8376−8388
Read Online

ACCESS | Metrics & More | Article Recommendations | Supporting Information

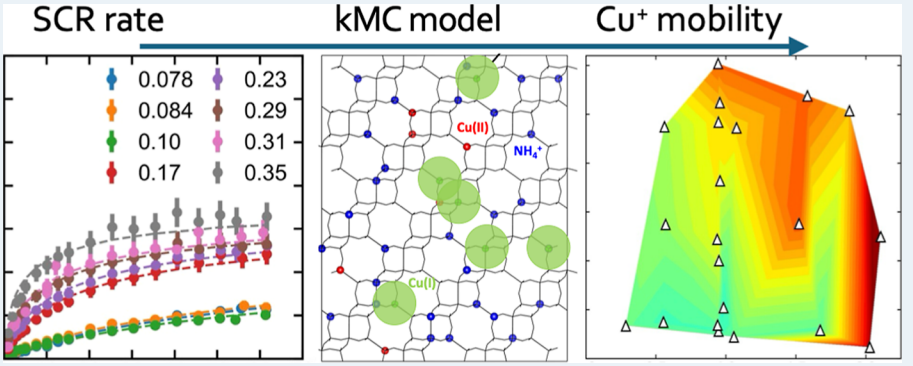

ABSTRACT: Copper-exchanged chabazite (Cu-CHA) zeolites are the preferred catalysts for the selective catalytic reduction of NO_x with NH_3. The low temperature (473 K) SCR mechanism proceeds through a redox cycle between mobile and ammonia-solvated Cu(I) and Cu(II) complexes, as demonstrated by multiple experimental and computational investigations. The oxidation step requires two Cu(I) to migrate into the same *cha* cage to activate O_2 and form a binuclear Cu(II)-di-oxo complex. Prior steady state and transient kinetic experiments find that the apparent rate constants for oxidation (per Cu ion) are sensitive to catalyst composition and follow nonmean-field kinetics. We develop a nonmean-field kinetic model for NO_x SCR that incorporates a composition-dependent Cu(I) volumetric footprint centered at anionic $[AlO_4]^-$ tetrahedral sites on the CHA lattice. We use Bayesian optimization to parameterize a kinetic Monte Carlo model against available experimental composition-dependent SCR rates and *in situ* Cu(II) fractions. We find that both rates and Cu(II) fractions of a majority of catalyst compositions can be captured by single oxidation and reduction rate constants combined with a composition-dependent Cu(I) cation footprint, highlighting the contributions of both Cu and Al densities to steady-state SCR performance of Cu-CHA. The work illustrates a pathway for extracting robust molecular insights from the kinetics of a dynamic catalytic system.

KEYWORDS: *Cu-CHA zeolites, NO_x selective catalytic reduction, dynamic active sites, kinetic Monte Carlo, Bayesian optimization*

INTRODUCTION

The selective catalytic reduction (SCR) of NO_x with ammonia

$$4NO + 4NH_3 + O_2 \rightarrow 4N_2 + 6H_2O \quad (1)$$

is commercially practiced for abatement of NO_x emissions from diesel and lean-burn engines. Copper-exchanged chabazite (Cu-CHA) zeolites are the most common catalysts for these applications because of their exceptional activity and hydrothermal stability over conditions relevant to exhaust after-treatment.[1−3]

The essential features of the Cu-CHA SCR catalyst system at low temperatures are well understood (Figure 1).[4,5] Copper cations are associated with anionic tetrahedral $[AlO_4]^-$ sites on the primarily siliceous CHA zeolite framework. In the Cu(II) state, those ions are nominally associated with either two $[AlO_4]^-$ as a so-called $Z_2Cu(II)$ or one $[AlO_4]^-$ as a $ZCu(II)OH$.[6−9] However, during low-temperature (<523 K) SCR conditions, NH_3 solvation liberates Cu cations from the zeolite framework, imparting mobility important to closing the Cu(I)/Cu(II) SCR redox cycle.[9−12] In the oxidation half-cycle, two Cu(I) ions selectively pair with O_2 to form a binuclear Cu(II) intermediate which in turn is reduced through reactions that consume NO and NH_3.

In steady-state kinetic experiments on Cu-CHA, low-temperature (473 K) SCR rates are observed to be approximately second-order with Cu density at low Cu loadings, evolving to a first-order dependence as Cu loadings

Received: March 29, 2024
Revised: April 25, 2024
Accepted: April 26, 2024
Published: May 14, 2024

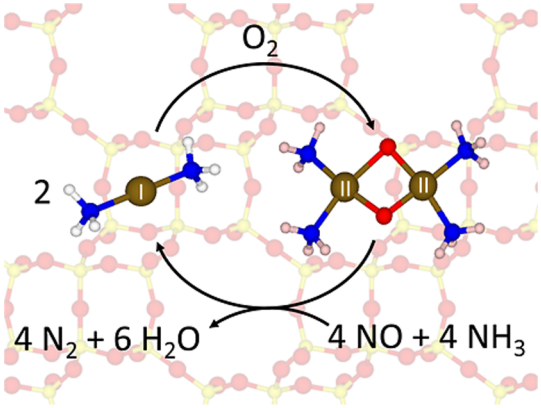

Figure 1. Schematic NO_x SCR mechanism. Brown, blue, red, yellow, and white spheres correspond to Cu, N, O, Si, and H atoms, respectively. Numerals indicate a formal Cu-oxidation state.

increase.[10,13−17] A similar compositional dependence is observed for SCR on other Cu-exchanged zeolite catalysts.[18] Steady-state SCR rates on CHA catalysts of a wide range of Cu compositions and Si/Al ratios exhibit a Langmuirian dependence on O_2 pressure.[16,17,19] Those kinetics are independent of *ex situ* Cu(II) ion speciation.[17] In *operando* X-ray absorption spectroscopy (XAS) measurements, steady-state Cu(II) fractions increase with increasing O_2 pressure irrespective of sample composition, reflecting the kinetic relevance of Cu(I) oxidation at low O_2 and Cu(II) reduction at high O_2 pressures.[16,17] Apparent rate constants in the oxidation (low O_2 pressure) and reduction (high O_2 pressure) limits have been extracted by fitting the steady-state SCR rates to an empirical Langmuir-type expression. At fixed volumetric Al density (Si/Al ratio) and at 473 K, the Cu-normalized oxidation rate constants vary nonlinearly with Cu density, as opposed to a strictly linear variation expected from mean-field second-order kinetic behavior expected from the mechanism of Figure 1, while reduction rate constants (per Cu) are invariant to Cu density.[16] In addition, at fixed Cu density (Cu/Al ratio), oxidation rate constants are observed to increase monotonically with Al density while reduction rate constants have a nonmonotonic dependence.[17] These observations reflect a composition sensitivity to SCR kinetics with a stronger sensitivity to the oxidation step. These findings are further supported by the observed composition-dependent apparent Cu(I) oxidation activation energy and compositionally invariant Cu(II) reduction apparent activation energy, especially at higher Cu loadings.[19]

The sensitivity of standard SCR kinetics at 473 K to Si/Al ratio and Cu loading suggests intrinsically nonmean-field behavior. Further evidence is provided by transient *operando* XAS experiments.[16,17] When samples are prepared in the oxidized [Cu(II)] state and subsequently exposed to flowing NO and NH_3, Cu(II) reduces to Cu(I) in a process that is first order in Cu and goes to completion, reflective of the apparent single-site kinetics. In contrast, samples prepared in the reduced [Cu(I)] and exposed to flowing O_2 are oxidized to Cu(II) in a process that is second order in Cu(I), consistent with the dual-site oxidation process.[10,15,20] The oxidation reaction, however, does not go to completion,[10,16,17] reflecting recalcitrant Cu(I) that can be rationalized as either spatially isolated from other Cu(I) or functionally isolated due to prior conversion of candidate partner Cu(I) to Cu(II).[10,17] In contrast, Cu(I) oxidation goes to completion in NO_2 independent of Cu composition, reflecting the single-site nature of this oxidation process.[10] *Ab initio* molecular dynamics simulations indicate that $Cu(I)(NH_3)_2$ are electrostatically attracted to anionic framework $[AlO_4]^-$,[4] are able to travel between the three *cha* cages sharing that $[AlO_4]^-$ with modest activation energy,[21] and are able to travel further from that $[AlO_4]^-$, through remote 8-membered rings into adjacent *cha* cages, with free energy barriers on the order of 60 kJ mol^{-1} depending on exact system details.[10,21] Comparison of observed recalcitrant Cu(I) are consistent with statistical predictions based on this assumed constrained mobility of $Cu(I)(NH_3)_2$ within and between adjacent *cha* cages.[17] Taken together, these observations underscore the contributions of zeolite composition, including Al and Cu densities and distributions, to observed low-temperature SCR kinetics.

A variety of macrokinetic and microkinetic models have been proposed for NO_x SCR on Cu-CHA. A number of phenomenological models treat SCR as a single lumped reaction with no explicit resolution of active sites.[22−25] Olsson *et al.*[26] proposed a global kinetic model with mechanistic steps occurring on three distinct but unspecified active site types distinguished by their ability to adsorb and store ammonia. Bendrich *et al.*[27] reported a macrokinetic model involving nitrite-assisted SCR reactions on Cu(II) sites but neglecting redox cycles involving Cu(I). Feng *et al.*[20] developed a mean-field, multisite microkinetic SCR model, parameterized against first-principles calculations, that was able to recover observed apparent activation energies and orders, but which contained no composition-dependent information. Daya *et al.*[28,29] incorporated further levels of granularity by advancing a Cu(I)/Cu(II) site-specific macroscopic redox kinetic model for SCR that was validated against observations from prior computational, transient kinetic, and spectroscopic studies. Despite the predictive utility of these models, they were based upon mean-field assumptions for all of the elementary steps. In light of a preponderance of experimental and computational evidence contradicting these assumptions for the NO_x SCR oxidation half cycle, it is desirable to construct and parameterize a kinetic model that accounts for the microscopic origins of the nonmean-field behavior and can simultaneously rationalize kinetic observations.

In this work, we explore the potential of physically based and microscopically consistent kinetic models that can capture prior measured isothermal (473 K) SCR kinetics[16,17] across a diverse catalyst compositional space with a minimum set of adjustable parameters. The reaction system is treated as a 3-dimensional CHA lattice, with Cu positions randomly assigned to tetrahedral (T)-site locations to a given catalyst composition. We compare a series of microkinetic models with increasing abilities to resolve microscopic details and examine their ability to capture and rationalize previously reported kinetic observations. We show that a mean-field microkinetic model that accounts for the dual-site nature of Cu(I) oxidation is unable to capture the composition dependence of NO_x SCR rates and Cu-oxidation state. We subsequently consider a coarse-grained, nonmean-field kinetic model with lumped Cu(II) reduction and Cu(I) oxidation steps, the latter incorporating a rate constant dependent on the proximity of Cu(I) pairs. This spatially resolved model is solved stochastically using kinetic Monte Carlo (kMC) for steady-state SCR rates and Cu(II) fractions. Bayesian

https://doi.org/10.1021/acscatal.4c01856
ACS Catal. 2024, 14, 8376−8388

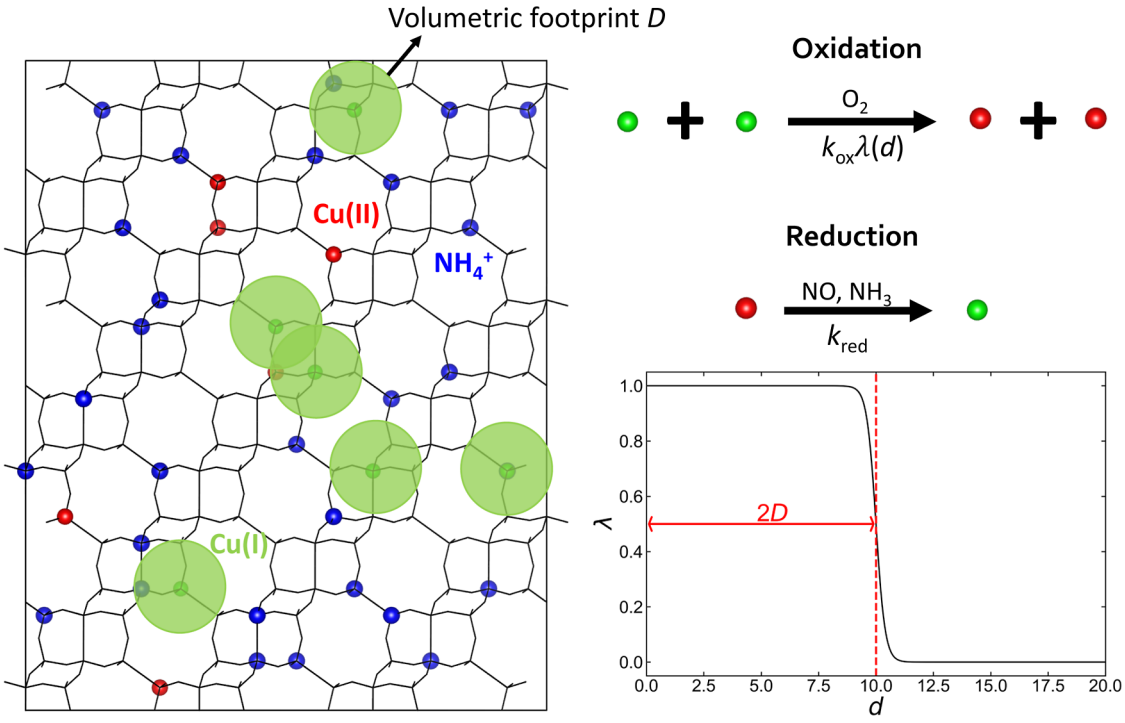

Figure 2. Spatially resolved kinetic model definition.

optimization is used to fit the nonanalytical kMC model to experimentally observed SCR rates and Cu(II) fractions. We show that a large body of experimental observations can be rationalized using a model that incorporates compositionally invariant oxidation and reduction rate constants along with a composition-dependent Cu(I) volumetric footprint. This footprint captures the composition-dependent mobility of Cu(I) and is shown to increase monotonically with Cu or Al density. These observations are consistent with prior experimental inferences regarding the influence of Cu and Al compositions on low-temperature SCR and elucidate the impact of altering cationic or anionic densities within Cu-CHA on its low-temperature SCR performance.

METHODS

Spatially Resolved Microkinetic Model. We consider a coarse-grained kinetic model for SCR constructed to be sensitive to catalyst composition- and O_2-pressure dependence.[16,17] A schematic of the model setup is shown in Figure 2. We begin with a CHA superlattice and substitute Al onto the framework to the desired Si/Al ratio, adhering to Löwenstein's rule forbidding first-nearest-neighbor $[AlO_4]^-$. We randomly assign Cu ions to the framework $[AlO_4]^-$ to the desired Cu/Al ratio (Cu density ρ_{Cu}). The Cu ions can interconvert between Cu(I) and Cu(II), as explained later. The residual Cu-free Al sites are treated as ammonium (NH_4^+) as appropriate for SCR conditions. We assume that the Cu ions occupy a spherical volumetric footprint of radius D, consistent with the symmetry around $[AlO_4]^-$ sites in the CHA lattice and *AIMD* evidence that Cu(I) can move nearly freely between the three equivalent cages shared by a tethering $[AlO_4]^-$ site.[21]

We decompose the SCR mechanism into lumped and dual-site Cu(I) oxidation and single-site Cu(II) reduction steps

$$2\mathrm{Cu(I)} \xrightarrow[k_{ox}\lambda(d)P_{O_2}]{O_2(g)} 2\mathrm{Cu(II)}$$
$$\mathrm{Cu(II)} \xrightarrow[k_{red}]{NO(g),NH_3(g)} \mathrm{Cu(I)} \quad (2)$$

where k_{ox} and k_{red} are effective oxidation and reduction rate constants, respectively, and the latter includes the lumped contributions of P_{NO} and P_{NH_3}, which we take as fixed. The oxidation rate includes a spatial dependence through $\lambda(d)$, where (d) is the separation between the two Cu(I) ions. We take $\lambda(d)$ to be isotropic and sigmoidal

$$\lambda(d) = \frac{1}{1 + e^{m(d-2D)}} \quad (3)$$

consistent with NH_3-solvation of Cu(I) and its ability to migrate between the three *cha* cages shared by a host Al with a low barrier. The volumetric footprint of a given Cu(I) is D, and the slope of the sigmoid at the point of inflection is m. The oxidation rate thus vanishes for Cu(I) pairs at separations greater than $2D$ and decays smoothly to zero as Cu(I) separations approach $2D$. The model becomes a mean field in the limit of large D (considered in detail in Section S2), and finite values of D capture the possibility of spatially isolated Cu(I), which is unable to participate in the SCR cycle. We set $m = 5$ to ensure a numerically stable and differentiable transition between the reactive ($\lambda = 1$) and nonreactive ($\lambda = 0$) regimes.

We solve this spatially resolved model using a rejection-free (Gillespie) kinetic Monte Carlo (kMC) algorithm[30,31] to compute steady-state rates and Cu(I)/Cu(II) fractions *vs* O_2 pressure and catalyst composition. All simulations are performed on a 26,244 T-site CHA supercell containing 2187 *cha* cages to facilitate adequate sampling even at dilute Cu or Al compositions. At a given reaction condition, kinetic quantities are estimated by averaging across 10 replicate

https://doi.org/10.1021/acscatal.4c01856
ACS Catal. 2024, 14, 8376−8388

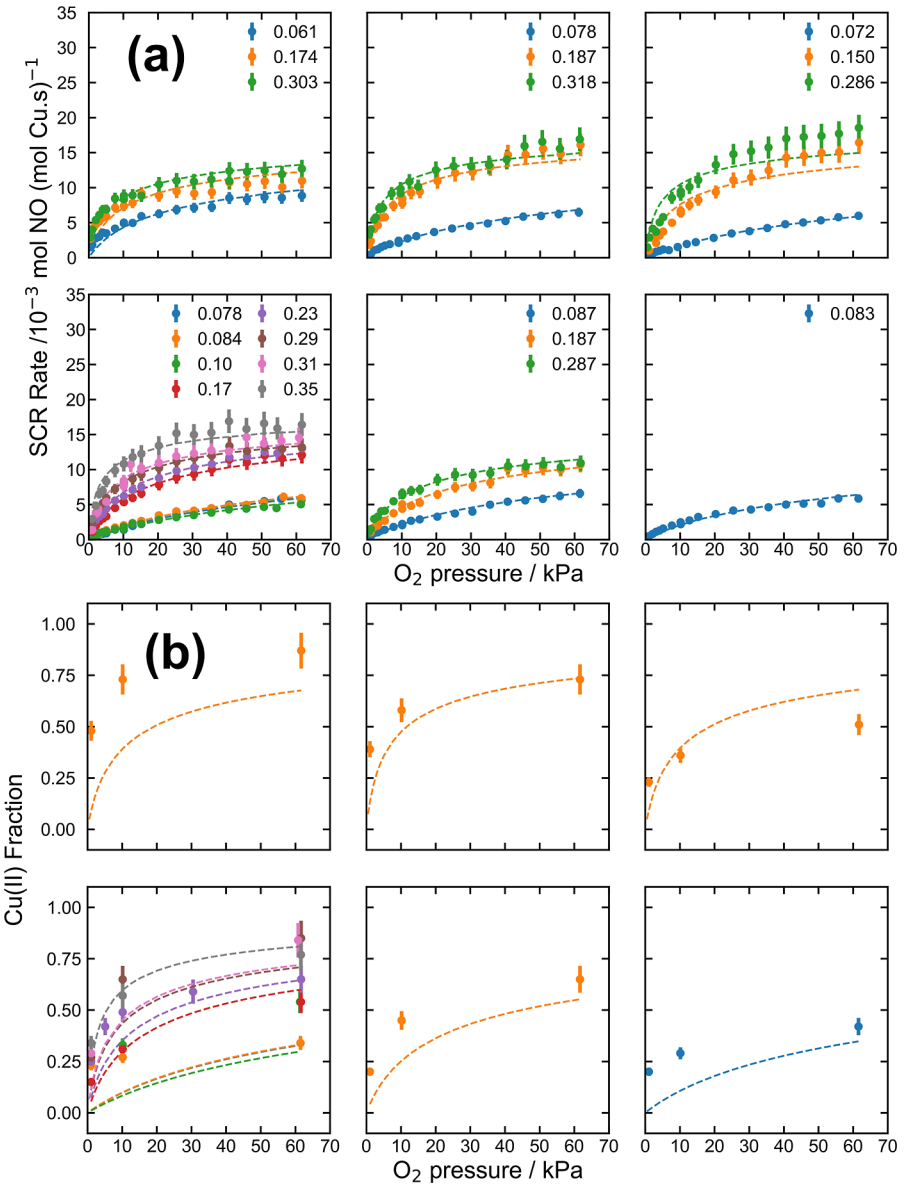

Figure 3. (a) Steady-state SCR rates *vs* O_2 pressure at Si/Al ratios of 6, 9, 13 (top row, left to right) and 20, 25, 50 (bottom row, left to right). Symbols and error bars indicate mean and 10% uncertainties in experimental observations. Legends report Cu density in Cu/(1000 Å^3). Dashed lines report *D*-only kMC model fits. (b) Same experimental and model results for XAS-estimated Cu(II) fractions. Experimental results adapted from refs 16 and 17.

simulations. The model is coded in Python and is available as an open-source Git repository.[32]

Bayesian Optimization. To fit k_{ox}, k_{red}, and D to experimental observations,[16,17] we define steady-state per Cu rate (r_{obj}) and steady-state Cu(II) fraction (f_{obj}) objective functions for a given catalyst composition ρ_{Cu} as

$$r_{obj}(k_{red}, k_{ox}, D) = \sum_{N_r} (R_{kMC}(k_{red}, k_{ox}, D; \rho_{Cu}, P_{O_2}) - R_{expt}(\rho_{Cu}, P_{O_2}))^2 \quad (4)$$

$$f_{obj}(k_{red}, k_{ox}, D) = \sum_{N_f} (x_{II,kMC}(k_{red}, k_{ox}, D; \rho_{Cu}, P_{O_2}) - x_{II,expt}(\rho_{Cu}, P_{O_2}))^2 \quad (5)$$

Here, R_{kMC} and R_{expt} are modeled and observed rates, respectively, and $x_{II,kMC}$ and $x_{II,expt}$ are modeled and observed Cu(II) fractions, respectively. N_r and N_f correspond to observations over discrete O_2 pressures. Minimization of r_{obj} and f_{obj} is not amenable to conventional least-squares approaches because the kMC models are nonanalytical and nondifferentiable. We thus recast it as a Bayesian optimization problem.

Bayesian optimization is suitable for global optimization of objective functions that are expensive to evaluate.[33] Briefly, a surrogate model for the objective is constructed, and a separate acquisition function is used to identify points in the parameter space predicted to be located near the global optimum. The objective function is evaluated at the proposed sampling points, which are then used as additional training data for the surrogate model and to generate new candidates through the acquisition function. This iterative sequence is continued,

https://doi.org/10.1021/acscatal.4c01856
ACS Catal. 2024, 14, 8376−8388

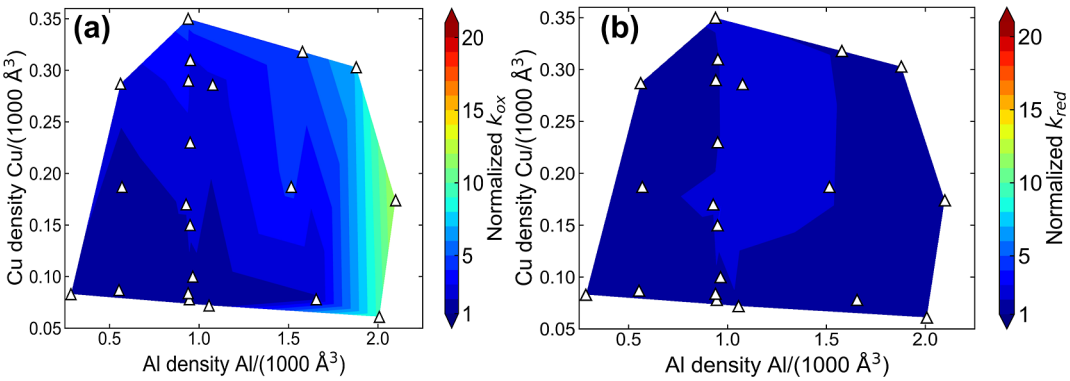

Figure 4. Sample compositions (data points) overlaid with contour maps of (a) normalized k_{ox} and (b) normalized k_{red} obtained by sample-wise second-order mean-field model fits against SCR rate data. Normalized to the least value of k_{ox} and k_{red}.

typically until a user-defined number of points has been sampled and the point with the most optimal objective value is chosen as the putative solution. Here, we treat the surrogate model as a single-output or multioutput Gaussian process using a Matern 5/2 kernel, depending on the type of optimization (single-objective/multiobjective) as will be discussed further. The Gaussian process prior was first initialized using Latin Hypercube Sampling[34] to generate 200 training points within the region $0 < k_{red} < 0.2$ mol_{NO} mol_{Cu}^{-1} s^{-1}, $0 < k_{ox} < 0.2$ mol_{NO} mol_{Cu}^{-1} s^{-1} $kPa_{O_2}^{-1}$ (1000 Å^3/Cu), and $0 < D < 60$ Å. For sampling, we employ an expected improvement acquisition function for single-objective optimization and an expected hypervolume improvement acquisition function[35,36] for multiobjective optimization. For the latter, the reference point was specified by adding a slight offset to the nadir point (objective-wise minimum) in the Pareto-optimal front (as suggested by Daulton *et al.*[35]), and sampling was done using nondominated partitioning along with a randomized quasi-Monte Carlo sampler. All optimizations were carried out using in-built implementations in the BoTorch[37] Python library. More than 200 sampling locations were considered for each optimization, and the objective functions were evaluated by averaging kinetic outputs from 10 parallel kMC simulations at each sampling location.

RESULTS AND DISCUSSION

Summary of the Experimental Data Set. We consider kinetic observations collected on Cu-CHA samples of varying Cu densities and Si/Al ratios of 6, 9, 13, 20, 25 and 50.[16,17] Steady-state SCR rates (per mol Cu, 473 K) were measured on each sample as a function of the O_2 pressure at 0.03 kPa NO, 0.03 kPa NH_3, 7 kPa CO_2, 1 kPa H_2O and balance N_2. In addition, for a subset of those samples, we consider *operando* XAS measurements of steady-state Cu(II) fractions at low (1 kPa), standard (10 kPa), and high (60 kPa) O_2 pressures. Figure 3 summarizes steady-state SCR rates (in mol_{NO} mol_{Cu}^{-1} s^{-1}) and XAS Cu(II) fractions as a function of O_2 pressure, at all sample compositions. As noted before,[16,17] SCR rates are consistently Langmuirian in O_2 pressure, and XAS-estimated Cu(II) fractions increase with O_2 pressure across all samples. These observations point to the kinetic significance of Cu(I) oxidation (at low O_2 pressures) and Cu(II) reduction half cycles (at high O_2 pressures). In addition, at a given Si/Al ratio, SCR rates increase with increasing Cu density.

Mean-Field SCR Model Parameterization. We explore multiple strategies to parameterize the mean-field model against the experimental data and investigate the prediction performance of each strategy. The experimental data in Figure 3 have previously been fit to a Langmuirian expression to extract apparent oxidation and reduction rate constants.[16,17,19] The Langmuirian treatment would be exact for truly single-site, mean-field oxidation and reduction behavior. A mean-field expression more consistent with the mechanism of Figure 1 can be derived from dual-site oxidation and single-site reduction steps (Section S2)

$$R_{MF} = k_{red}\left(1 - \frac{\sqrt{k_{red}^2 + 8k_{ox}k_{red}\rho_{Cu}P_{O_2}} - k_{red}}{4k_{ox}\rho_{Cu}P_{O_2}}\right) \quad (6)$$

$$x_{II,MF} = 1 - \frac{\sqrt{k_{red}^2 + 8k_{ox}k_{red}\rho_{Cu}P_{O_2}} - k_{red}}{4k_{ox}\rho_{Cu}P_{O_2}} \quad (7)$$

Here, R_{MF} is the mean-field per Cu rate, and $x_{II,MF}$ is the corresponding mean-field Cu(II) fraction. Unlike the Langmuirian expression (eq S3), eq 6 naturally incorporates a Cu density dependence. We first explored the ability of this expression to describe the SCR rate data set (Figure 3a) with single values of k_{ox} and k_{red}, by minimizing the sum of squared errors between observed and modeled mean-field rates across all sample compositions and oxygen pressures using the nonlinear regression capabilities in SciPy

$$r_{obj,MF}(k_{ox}, k_{red}) = \sum_{samples}\sum_{P_{O_2}} (R_{MF}(k_{red}, k_{ox}; \rho_{Cu}, P_{O_2}) - R_{expt}(\rho_{Cu}, P_{O_2}))^2 \quad (8)$$

Optimal k_{ox} and k_{red} are 0.002 mol_{NO} mol_{Cu}^{-1} s^{-1} $kPa_{O_2}^{-1}$ (1000 Å^3/Cu) and 0.024 mol_{NO} mol_{Cu}^{-1} s^{-1}, respectively. The corresponding rate fits and predicted Cu(II) fractions are shown as dashed lines in Figure S1. It is evident that the model does a poor job of capturing the full data set. To quantify fit quality and bias, we evaluated root mean squared percentage error (RMSPE) and mean percentage error (MPE), respectively. Figure S2 reports both rate and Cu(II) fraction errors across all of the samples. Rate RMSPE ranges from 10 to 90%, and MPE reports both positive and negative biases. Cu(II) fraction RMSPE is greater than 50% and uniformly negatively biased across all samples. We conclude that a single mean-field model is unable to describe the SCR data set.

https://doi.org/10.1021/acscatal.4c01856
ACS Catal. 2024, 14, 8376−8388

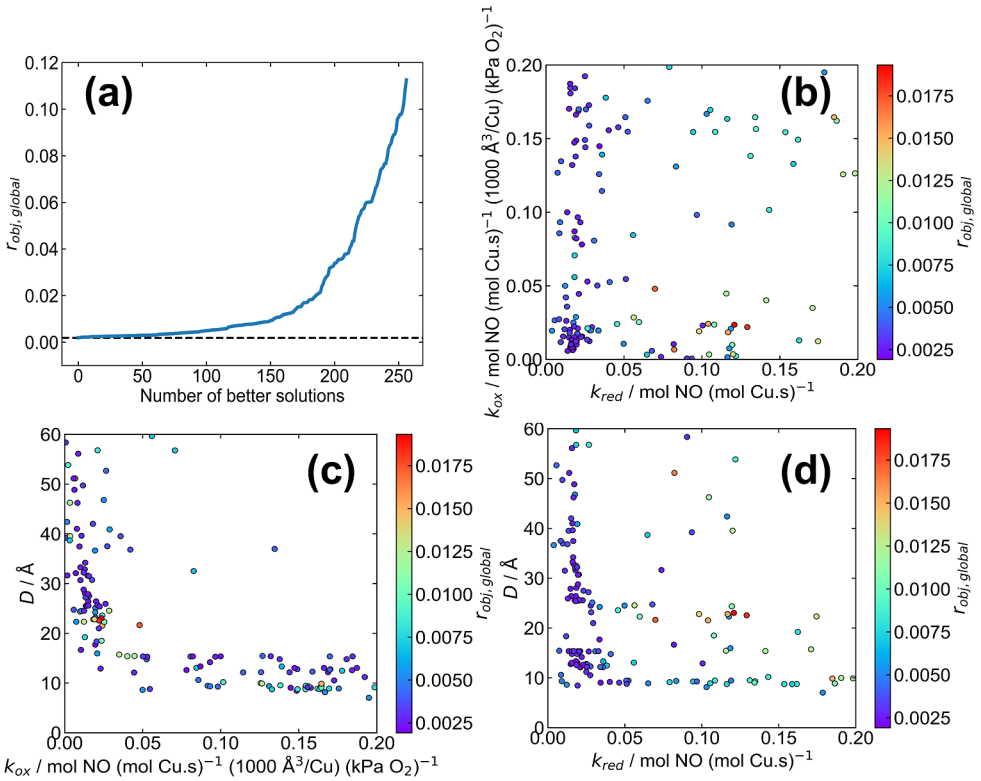

Figure 5. (a) Cumulative solution distribution of r_{obj} from global. Horizontal dashed line indicates second-order mean-field model r_{obj}. (b–d) Scatter plots of k_{ox} *vs* k_{red}, D *vs* k_{ox}, and D *vs* k_{red} within 10% of the least sampled objective, respectively. Points color-coded by r_{obj}.

We next regressed eq 6 against the individual sample SCR rates. Figure S3 reports the regressed rate fits and corresponding predicted Cu(II) fractions. The corresponding sample-wise fit quality and bias metrics are shown in Figure S4. The RMSPE values for the SCR rates are predictably lower than the global case due to an increase in the total model degrees of freedom (two per sample). Model biases are mostly negative for all samples and smaller in magnitude relative to the global fit. The predicted Cu(II) fraction exhibits lower RMSPE relative to the global, although the model consistently underpredicts observed fractions.

Regressed k_{ox} and k_{red} normalized to their minimum values [0.001 $mol_{NO}\ mol_{Cu}^{-1}\ s^{-1}\ kPa_{O_2}^{-1}$ (1000 Å^3/Cu) and 0.011 $mol_{NO}\ mol_{Cu}^{-1}\ s^{-1}$, respectively] are reported as contour plots *vs* Cu and Al density in Figure 4. k_{red} varies by about a factor of 2 across compositions and k_{ox} by a factor of 12. Variations are stronger with Al than with Cu density, reflecting the lurking contribution of Al density not captured in the simple mean-field model. Variations in rate constants are qualitatively consistent with those extracted from the Langmuirian expression (eq S3),[16,17] although absolute variations across composition are significantly larger (factors of 3 and 18 for reduction and oxidation, respectively) in the Langmuir fits (Figure S5). Thus, the Cu density dependence in the second-order model does appear to capture some, but not all, of the physics of the real system.

kMC-Based SCR Model Parameterization. Here, we explore multiple methodologies to parameterize the 3 parameter spatially resolved kMC model (k_{ox}, k_{red}, D) against the experimental data and compare their corresponding fitting performances. We first explored the ability of the model to capture the experimental rate data set (Figure 3a) across all samples with a global set of parameters using Bayesian optimization to minimize eq 4 across all sample compositions and O_2 pressures. Figure 5a reports the cumulative distribution of sampled solutions ranked by r_{obj}. The dashed line corresponds to r_{obj} from the global second-order mean-field model. The mean-square error from the most optimum sampled solution is slightly below this objective value, indicating that the inclusion of the volumetric footprint D only marginally improves the ability to describe the experimental data. In addition, the asymptotic behavior near $x = 0$ better solutions indicates the existence of multiple sampled solutions with similar and optimum fit performance. This observation is further supported by the pair scatter plots of sampled solutions within 10% of the least sampled objective shown in Figure 5b–d. Solutions of similar r_{obj} are scattered throughout the parameter space, suggesting that the global kMC model is overfitting the experimental data set. Figure S6 reports the prediction performance of the kMC model using the parameter set with the least sampled objective against the corresponding experimental rate and fraction data, and Figure S7 reports the corresponding fit performance metrics. SCR rate RMSPE is up to 100% and nonsystematic, while Cu(II) fraction RMSPE is similarly large and negatively biased.

These findings show that a unique global kMC parameter set does not exist. Further, it appears that the rate data set alone is insufficient to uniquely parameterize the model. To test this latter point, we regressed the kMC model against the rate data set of a sample with median Cu and Al density (ρ_{Cu} = 0.23 Cu/1000 Å^3 and Si/Al = 20). Figure S8a reports the solution distribution, and Figure S8b–d shows the corresponding pairwise solution scatter plots. A large number of solutions have similar and small r_{obj}. Further, optimal k_{ox} and D appear to be correlated, reflecting a model that is underdetermined.

https://doi.org/10.1021/acscatal.4c01856
ACS Catal. 2024, 14, 8376–8388

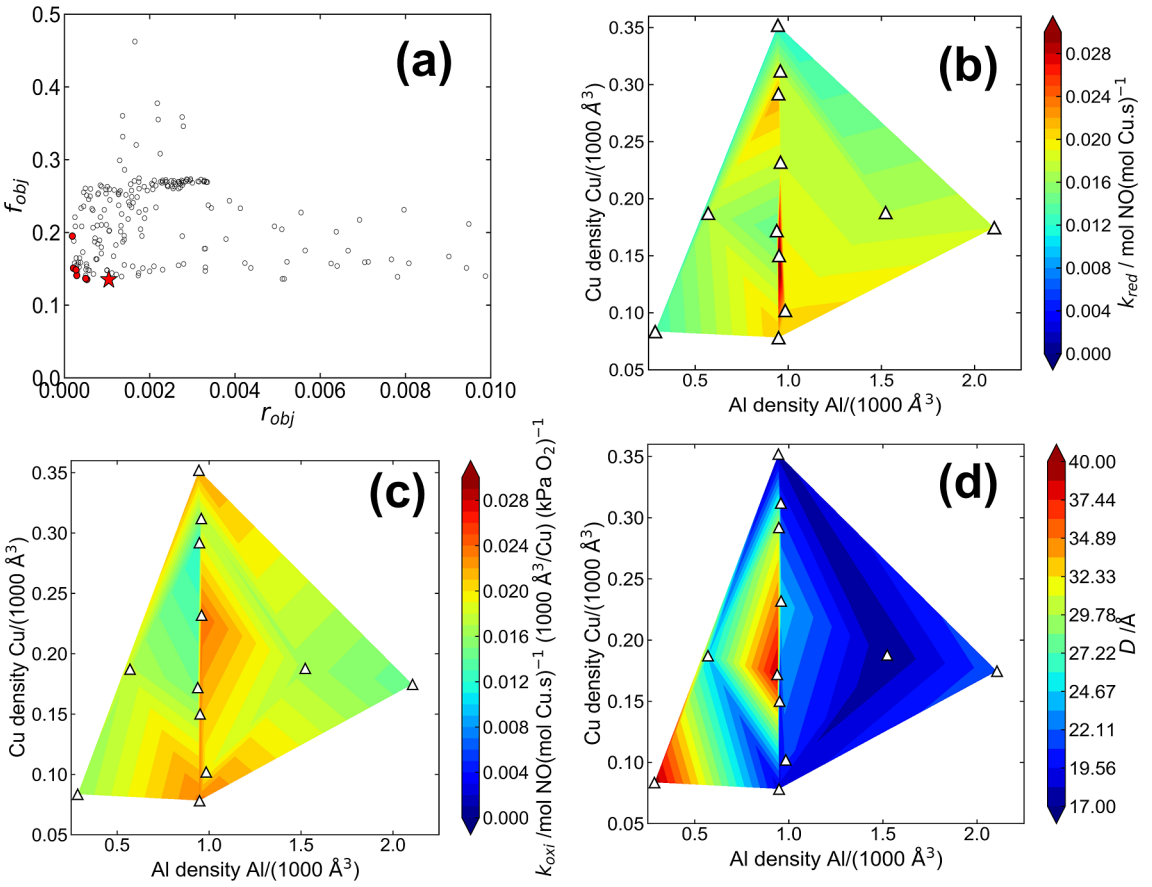

Figure 6. (a) Sampled r_{obj} and f_{obj} from multiobjective Bayesian optimization of ρ_{Cu} = 0.23 Cu/1000 Å^3 and Si/Al = 20 Cu-CHA sample. Pareto-optimal points are colored in red. The star indicates the least normalized Euclidean distance from the origin solution. (b) k_{red}, (c) k_{ox}, and (d) D contour maps *vs* Cu and Al densities. Experimental sample compositions indicated with triangles.

These observations motivate incorporation of the XAS-estimated Cu(II) fraction data set (Figure 3b) into the kMC model parameterization. We turn to multiobjective Bayesian optimization to simultaneously minimize r_{obj} (eq 4) and f_{obj} (eq 5) across samples for which both data sets are available. A scatter plot of results for a sample of composition Si/Al = 20 and ρ_{Cu} = 0.23 Cu/1000 Å^3 is reported in Figure 6a. r_{obj} points range to near zero, while f_{obj} points are systematically greater than 0.12. Scatter plots for multiobjective Bayesian optimization of other select Cu-CHA samples are reported in Figure S9 and behave similarly.

We chose as representative solutions for each sample the one with the least normalized Euclidean distance from the origin

$$d_{Euclid} = \sqrt{(r_{obj}/r_{max})^2 + (f_{obj}/f_{max})^2} \quad (9)$$

and estimated parameter uncertainties by considering the standard deviation in sampled parameter sets with Euclidean distances within 10% of the representative solution. Figure S10 reports representative solutions and corresponding uncertainties for k_{ox}, k_{red}, and D across all samples. The parameter uncertainties are markedly less than those from the kMC model regressed against rate data sets only. Figure S11 reports the representative solution fits against the experimental data, and Figure S12 reports the corresponding regression metrics. Both rate and Cu(II) fraction RMSPE are substantially decreased relative to the global fits. Further, the prediction biases indicated by MPE are closer to zero, especially for the Cu(II) fractions, with the model continuing to mostly underpredict the experimental fractions.

The composition-dependence of the representative k_{ox}, k_{red}, and D are shown as contour maps in Figure 6b–d, respectively. Variations in k_{red} and k_{ox} are a factor of about two across compositions, significantly less than the variations reported by the second-order mean-field model fits. On the other hand, D varies more dramatically with composition. The standard deviation in D is 30% across all compositions, compared to 16% for both k_{ox} and k_{red}. Thus, the Cu volumetric footprint D appears to be capable of capturing most of the composition dependence in SCR rates and Cu(II) fractions.

These observations suggest that the entire data set may be captured by a smaller number of adjustable parameters. We first considered the consequences of varying the model parameters one at a time between the maximum and minimum of the regressed values in Figure 6b–d, holding the remaining parameters fixed at the mean of their regressed values. For each parameter set, kMC-computed SCR rates *vs* O_2 pressure were computed at ρ_{Cu} = 0.23 Cu/1000 Å^3 and Si/Al = 20. Figure S13a–c shows rate sensitivities to each parameter, and Figure S13d reports the ratio of the SCR rates for the respective parameter variations as a function of the O_2 pressure. Rates are most sensitive to variations in D, with SCR rate ratios varying from six at low and low O_2 pressures to two at high and low O_2 pressures.

We subsequently considered whether a composition-dependent D alone could describe the entire data set. We

https://doi.org/10.1021/acscatal.4c01856
ACS Catal. 2024, 14, 8376−8388

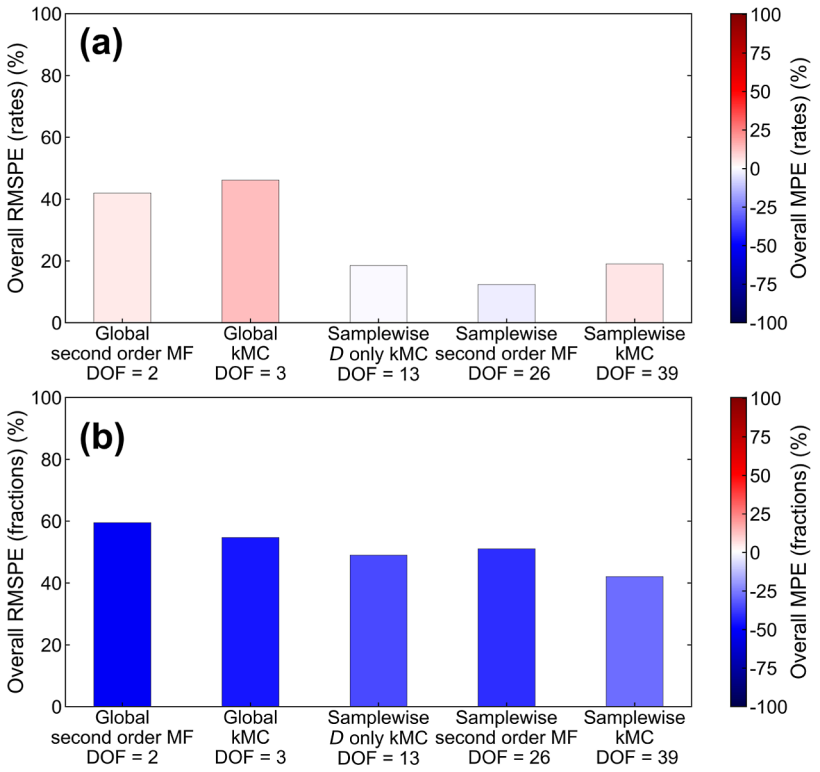

Figure 7. (a) Overall root-mean-square predictive error (RMSPE) and mean percentage error (MPE) against experimental rates and (b) overall RMSPE and MPE against experimental Cu(II) fractions for all regression and modeling strategies considered. "DOF" reports the degrees of freedom in each model.

fixed k_{ox} and k_{red} at their mean values of 0.018 $mol_{NO}\ mol_{Cu}^{-1}\ s^{-1}\ kPa_{O_2}^{-1}$ (1000 Å^3/Cu) and 0.018 $mol_{NO}\ mol_{Cu}^{-1}\ s^{-1}$, respectively. These rate constants are quantitatively similar to those extracted from transient kinetic experiments[16,17] (±0.02 corresponding units for both). In addition, they are of the same order of magnitude as the apparent rate constants estimated by Gao *et al.*[14,15] for SCR on Cu-CHA at 473 K, 10 kPa O_2, 0.035 kPa NO, and 0.035 kPa NH_3, conditions consistent with the steady-state kinetic experiments in Figure 3. Figure 3 shows the regressed model rate fits and inferred Cu(II) fractions compared with experimental data. The corresponding fit metrics for both fraction and rate data sets are shown in Figure S14. The model, in general, is able to capture the experimental rate observations within 20% RMSPE. Modeled Cu(II) RMSPE fractions are less than 50% for most samples but again underpredict the experimental observations.

Figure 7 compares the rate and Cu(II) fraction RMSPE and MPE for each model, aggregated across samples for which both data sets are available. Sample-wise models provide significantly better rate predictions than global models. Further, a kMC model with fixed k_{ox} and k_{red} and variable D has an RMSPE comparable to the sample-wise kMC model and nearly as small as the sample-wise mean-field second-order fit, with one-third to one-half as-many adjustable parameters. Further, this model has the smallest rate MPE, indicating the smallest bias in rate predictions. Cu(II) fraction RMSPE are considerably larger across all models and have systematically negative MPE. The sample-wise kMC model, with the largest number of degrees of freedom [39, considering the 13 samples for which both rate and Cu(II) fraction data are available], has the smallest RMSPE, but performs only marginally better than the variable D-only model. These large and systematic errors in the Cu(II) fraction could have several origins, including (a) insufficient fraction observations to regress the kMC models; (b) physical flaws with the kMC model itself; or (c) systematic errors in observation or interpretation of the experimentally measured Cu(II) fractions.

Close inspection of Figure 3a shows that the variable volumetric footprint model performs particularly poorly at high O_2 pressure (reduction-limited rates) for two Si/Al = 6 and two Si/Al = 13 samples. Rate RMSPE values for these four samples exceed 25%, as shown in Figure S14a. We fixed k_{ox} to 0.018 $mol_{NO}\ mol_{Cu}^{-1}\ s^{-1}\ kPa_{O_2}^{-1}$ (1000 Å^3/Cu) and refit k_{red} and D against the rate data for these four compositions. Including k_{red} as an additional fit parameter improves the high-pressure kinetic predictions and overall regression performance. Comparison of this refit k_{red} to the global fit value shows that the refit Si/Al = 6 and Si/Al = 13 k_{red} are systematically less and greater than the global fit, respectively. This sensitivity of k_{red} to Al density at fixed Cu density reflects a likely secondary influence of spectator NH_4^+ on SCR reduction rate constants.[17] Table S1 summarizes the variable volumetric footprint parameters for all samples, incorporating the refit values for these four samples.

Physical Interpretation of *D*. As shown in Figure 2, D can be interpreted as the effective diameter visited by solvated Cu(I) relative to its anchoring Al site. The analysis of kinetic data indicates that the variable volumetric footprint model provides the best balance between model performance and minimization of parameters. We next consider the potential to extract physical insight from the composition-dependence of D.

https://doi.org/10.1021/acscatal.4c01856
ACS Catal. 2024, 14, 8376−8388

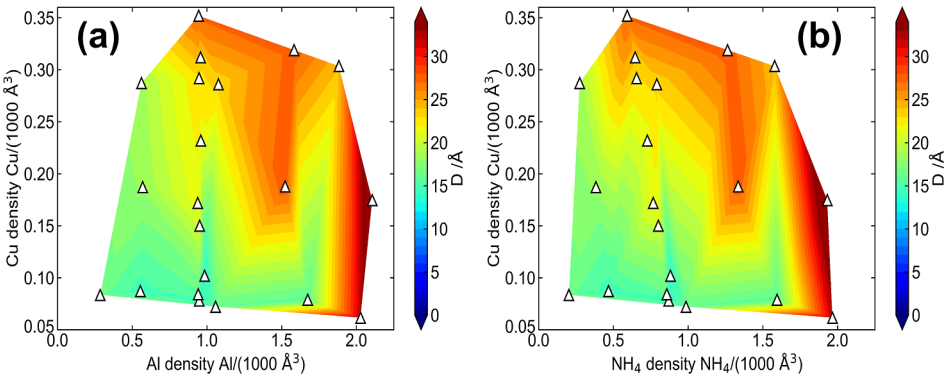

Figure 8. Filled contour map of volumetric footprint D from Table S1 against (a) Cu and Al density and (b) Cu and NH_4^+ density. Data points correspond to sample compositions. Intermediate points were evaluated using linear interpolation on a 1000 × 1000 triangular grid.

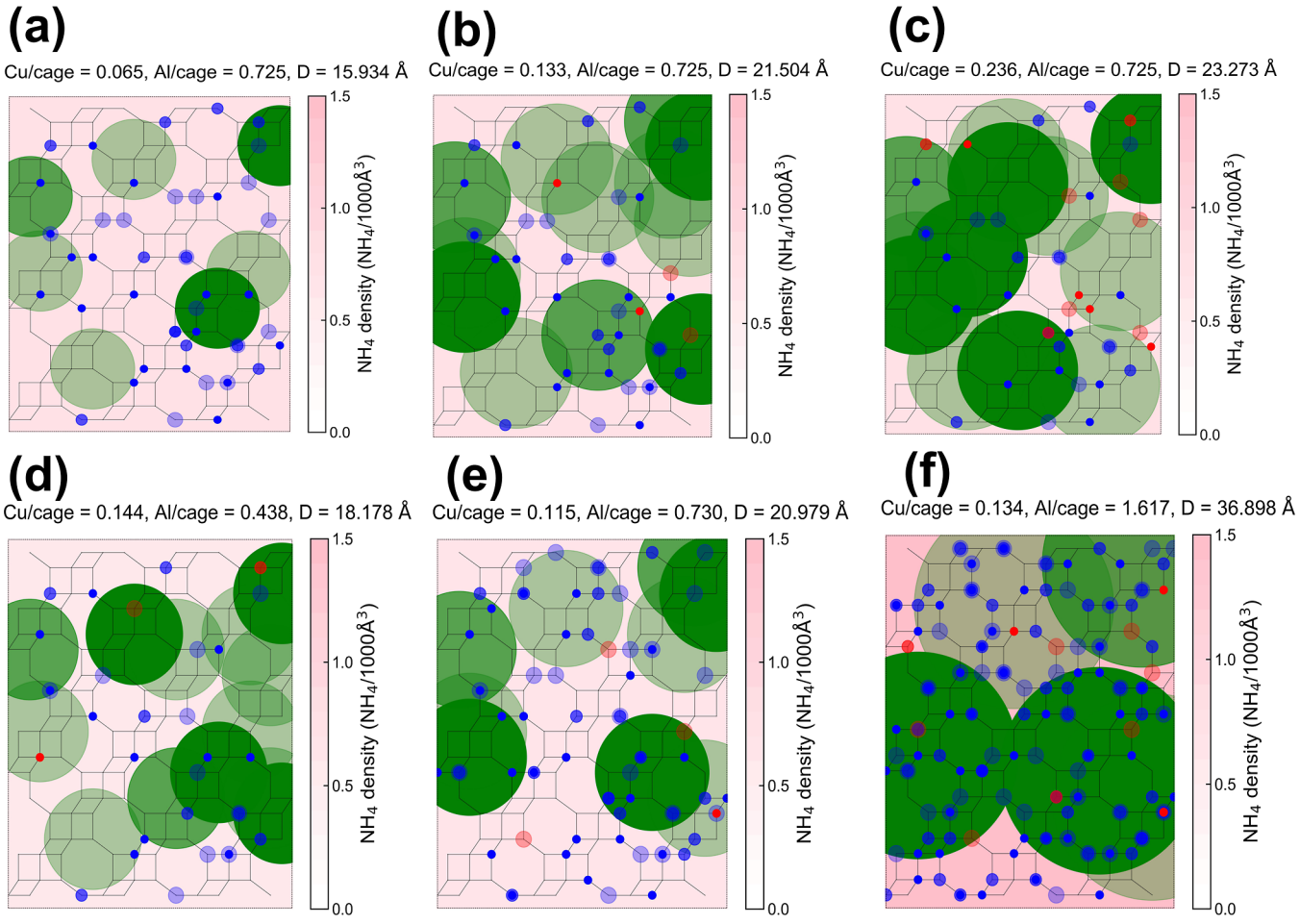

Figure 9. Steady-state snapshots, projected along **a** lattice vector, of a 3 × 3 × 3 portion of the kMC supercell evaluated at 10 kPa O_2 pressure. Top row: Al density ≈0.25 Al/1000 Å^3 and Cu densities of (a) 0.08, (b) 0.23, and (c) 0.31 Cu/1000 Å^3. Bottom: Cu density ≈0.17 Cu/1000 Å^3 and Al densities of (d) 0.56, (e) 0.94, and (f) ≈1.52 Al/1000 Å^3. Red and blue markers indicate Cu(II) and Al, respectively, with increasing size and transparency along the **a** direction. Green markers represent Cu(I) with size proportional to volumetric footprint D and transparency increasing along the **a** direction. Background color indicates the ammonium density.

The D values reported in Table S1 are plotted as filled contour maps against Cu and Al density in Figure 8a and against Cu and NH_4^+ density [taken as the difference between Al and Cu density, thus capturing the fraction of Cu-free Brønsted sites in the limit of complete reduction to Cu(I)] are shown in Figure 8b. The volumetric footprint increases systematically with both Cu(I) and Al (or NH_4^+) density with greater sensitivity to the latter. Values range between 14 Å, comparable to the distance between two six-membered rings within a *cha* cage, and 36 Å, encompassing the furthest center-to-center distance between six-membered rings of the first nearest neighboring *cha* cages (Figure S17). At its greatest extent, the Cu(I) footprint thus appears to extend to adjacent *cha* cages, consistent with metadynamics simulations[10,21] as well as with statistical analyses of the maximum oxidizable Cu(I) in transient oxidation experiments.[17,18]

https://doi.org/10.1021/acscatal.4c01856
ACS Catal. 2024, 14, 8376−8388

To illustrate the influence of the finite volumetric footprint on the fraction of Cu participating in SCR, we compare in Figure S19 the fraction of Cu(II) predicted from the kMC model at 60 kPa_{O_2} with that from the mean-field model at the same conditions and identical kinetic parameters. While the mean-field model predicts nearly 100% Cu(II) at high P_{O2}, the kMC value varies from about 40 to 80% depending on catalyst composition. Thus, the finite footprint can have a substantial impact on the fraction of Cu sites utilized (or participating in) SCR redox cycles.

To illustrate the physical implications of D, Figure 9 shows snapshots drawn from the steady-state kMC simulations at 10 kPa_{O_2}. We extract a 3 × 3 × 3 portion of the larger 9 × 9 × 9 CHA supercell (Figure S18) and project along the **a** lattice vector. Green spheres represent Cu(I) in sizes proportional to their volumetric footprint; blue and red sites represent NH_4^+ and Cu(II), respectively. Snapshots are drawn from three samples with low (≈0.08 Al/1000 Å^3), medium (≈0.23 Al/1000 Å^3), and high (≈0.31 Al/1000 Å^3) Cu densities at fixed Al density and three samples with low (≈0.56 Al/1000 Å^3), medium (≈0.94 Al/1000 Å^3), and high (≈1.52 Al/1000 Å^3) Al densities at fixed Cu. With an increase in either density, the volumetric footprint of the Cu increases. The ammonium density appears to control the footprint to a greater extent than the Cu density. This may be due to a larger increase in the number of Al cohosted with Cu when Al density is increased at fixed Cu density, as compared to an increase in the number of Cu cohosted with Cu when Cu density is increased at fixed Al density.

To make the connection to cage separation more explicit, we considered the distribution of framework Al−Al separations (as a surrogate for Cu travel distance) using a previously reported titration model.[17] Briefly, we distribute Al onto the CHA framework attending to Löwenstein's rule up to a target Si/Al ratio and then randomly populate Al with Cu to the desired Cu/Al ratio. We then sequentially titrate Cu pairs that share the same *cha* cage, followed by Cu pairs that are in adjacent *cha* cages separated by one 8-membered ring, and so on. We record the Al−Al separation during this titration procedure for low (0.078 Cu/1000 Å^3), medium (0.23 Cu/1000 Å^3), and high (0.35 Cu/1000 Å^3) Cu compositions at Si/Al = 20. Statistics were gathered through 10,000 parallel simulations carried out on a 36 T supercell obtained from the IZA[38] and repeated 9 times along each lattice vector. Figure 10 reports the probability density distribution of pair distances at each cage separation. The structure observed in the "same cage" distribution reflects the contribution of the underlying crystallography, which is reduced at greater cage separations. Corresponding optimized D values from Table S1 are indicated as vertical dashed lines. From a comparison of the two, migration of Cu between neighbor and even second neighbor cages may contribute to SCR. The picture also highlights a fundamental limitation of the kMC model, which assigns equal rates to all Cu pairs, regardless of relative cage proximity. A more sophisticated model could distinguish the contributions of these different events to overall rates, although as we have seen above, the available data are insufficient to parameterize or validate a finer-grained model.

While this analysis considers the consequences of Cu separations, it does not account for the consequences of colocated NH_4^+ on the oxidizable Cu fraction. However, as reported in Figure 8b, the volumetric footprint is sensitive to

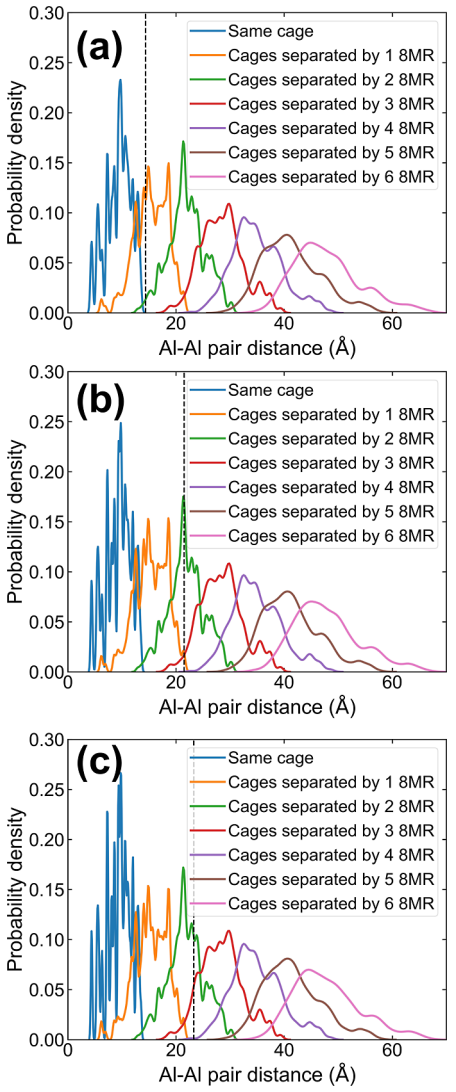

Figure 10. Probability density distributions of titrated Al−Al pair distances across iteration sequences, collected for Cu-CHA samples at Si/Al = 20 and Cu densities of (a) 0.078 Cu/1000 Å^3, (b) 0.23 Cu/1000 Å^3, and (c) 0.31 Cu/1000 Å^3. Vertical dashed lines indicate regressed D for the corresponding sample.

both Cu and NH_4^+ density. This suggests that the Cu(I) footprint is linked to its microenvironment, in particular the amount of colocated Cu(I) and NH_4^+ cations located in its vicinity. To elucidate the relationship between D and the compositional structure, for every studied composition, we populate Al, Cu, and NH_4 on the CHA lattice using the above procedure. We subsequently compute the conditional probabilities

$$P(\mathrm{Cu|Cu}) = \frac{P(\text{cage containing at least 2 Cu})}{P(\text{cage containing Cu})} \tag{10}$$

$$P(\mathrm{NH_4|Cu}) = \frac{P(\text{cage containing Cu and at least 1 NH}_4)}{P(\text{cage containing Cu})} \tag{11}$$

The dependence of D on these two conditional probabilities is presented as a contour map in Figure 11. D generally increases with both probabilities and is more sensitive to $P(\mathrm{NH_4|Cu})$, the conditional probability of coresidence of NH_4 and Cu in

https://doi.org/10.1021/acscatal.4c01856
ACS Catal. 2024, 14, 8376−8388

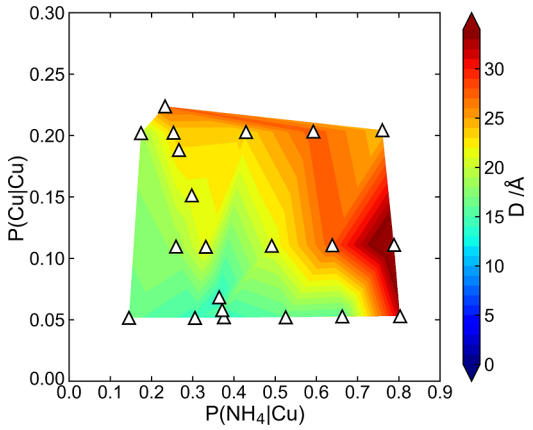

Figure 11. Regressed D (including corrections for outliers) as a filled contour map against $P(\mathrm{Cu|Cu})$ and $P(\mathrm{NH_4|Cu})$. Data points correspond to sample conditional probabilities. Intermediate points were evaluated through linear interpolation within a 1000 × 1000 triangular grid.

the same cage. This suggests that the presence of another cation (in particular, NH_4) within the same cage increases the volumetric footprint of Cu(I) on average. With the increasing occurrence of colocated cationic species, electrostatic repulsions between may enable Cu(I) to travel further on average, as inferred from umbrella sampling simulations.[21] Gao and coworkers[39] used *operando* electron paramagnetic resonance (EPR) to estimate Cu ion dynamics as a function of Cu loading during low-temperature SCR. They found that increasing the Cu density raises ion mobility, in agreement with the above findings. This further underscores the connection between Cu(I) mobility and its local electrostatic environment. Because each cation is associated with anionic $[AlO_4]^-$, it appears that higher concentrations of anionic Al centers within a cage increase the mobility of Cu(I), in agreement with findings from Krishna *et al.*[17] Recently, Millan *et al.*[40] performed machine-learned molecular dynamics simulations studying the motion of Cu(I) species in CHA across a range of Si/Al ratios and Cu densities. They demonstrated that the probability of colocated Cu(I) increases with Cu and Al loading, in agreement with our findings.

CONCLUSIONS

The practically significant chemistry of NO_x reduction by NH_3 on Cu−zeolites presents unique fundamental challenges to linking microscopic and macroscopic behavior. While considerable experimental and computational effort has been directed at determining the elementary steps of NO_x SCR over Cu-exchanged zeolites,[12,20,27] the dependence of mechanism and rates on catalyst compositional variables has received less attention.[14] Kinetic inferences have relied on extrapolations of steady-state SCR rate data to oxidation- and reduction-limited regimes that do not exploit the complete set of kinetic information and provide microscopic insights only indirectly.[16,17,19] Here, we consider a molecularly consistent model, which treats oxidation and reduction half-cycles as single steps and extracts physical insights through comparison against a full data set of composition-dependent kinetics. While a mean-field model based on first-order (in Cu) reduction and second-order (in Cu) oxidation half-reactions is unable to rationalize observed rates and Cu(II) fractions across a space of catalyst compositions, the introduction of an explicit and composition-dependent Cu(I) mobility parameter does allow both to be captured with good reliability across a large number of samples. Intrinsic oxidation and reduction rate constants correspond well with other reports. Further, the inferred mobility of Cu(I) is of the order of two *cha* cages, consistent with statistical and computational predictions, and is an increasing function of total cation density, including both Cu and NH_4^+ ions. The model rationalizes a large body of experimental results and provides microscopic insights into the material and mechanistic factors that control low-temperature SCR kinetics in Cu-CHA.

While the apparent homogeneous-like nature of active sites involved in low-temperature, Cu−zeolite-catalyzed NO_x SCR has been highlighted,[15] experimental data and computational models show that the behavior is more nuanced. Solvated Cu(I) ions are mobile, but their kinetic behavior is sensitive to framework Al density, indicating that they retain some memory of their tethering to the anionic zeolite framework, thus adopting some but not all characteristics of a heterogeneous catalyst. Because the underlying low-temperature NO_x SCR mechanism cannot be described using mean-field kinetics, a stochastic kinetic Monte Carlo algorithm is necessary to parameterize and solve the reaction network. In the context of heterogeneous catalysis, kinetic Monte Carlo is most often applied to reaction networks on extended planar surfaces, which can take advantage of the reduced dimensionality and long-ranged order of an underlying, typically metal, lattice to simplify parameterization.[41,42] The absence of long-ranged Al site ordering on the CHA lattice, the existence of multiple, differentially mobile, charge-compensating ions, and their collective influence on the reaction mechanism considerably complicate a first-principles-based parameterization of a complete kinetic model. This complexity motivates our approach here, of Bayesian optimization of the reduced nonmean-field model against the experimental data. We learn that rate data alone are insufficient to parameterize the model, and that secondary *operando* (under reaction conditions) information about the catalyst state (fractions of reduced and oxidized Cu ions) is needed to determine even this simplified model. Further, this approach provides a direct connection between observed macroscopic kinetics and underlying physical behavior, in this case, the apparent mobility of Cu(I) ions. Validation of a more microscopically complete, even microkinetic, NO_x SCR mechanism would thus require additional *operando* information, for instance, additional rate orders or quantifications of other intermediates or kinetic rate constants obtained through transient oxidation/reduction experiments. First-principles models could well inform a more complete model, for instance, providing a more accurate representation of Cu(I) mobility, although it is revealing that even the very simple, "muffin-tin" model used here captures observed behavior satisfactorily.

While the community has recognized dynamic active site behavior that cannot be described by mean-field heterogeneous or homogeneous kinetic models (especially, but not exclusively, in metal−zeolite systems),[43] we currently lack molecularly consistent models to describe and interpret these observations as a function of reaction conditions and material composition. The framework illustrated here is a step forward in developing physically realistic and interpretable models that capture the observed kinetic behavior. It highlights the importance of careful integration of experiments and theory to arrive at robust molecular insights for dynamic systems.

https://doi.org/10.1021/acscatal.4c01856
ACS Catal. 2024, 14, 8376−8388

■ ASSOCIATED CONTENT

Supporting Information

The Supporting Information is available free of charge at https://pubs.acs.org/doi/10.1021/acscatal.4c01856.

Derivation and application of mean-field expressions to SCR kinetics, rate and Cu(II) fraction fits/predictions for all considered parameterization methods and corresponding fit performance metrics, and regressed kMC model parameters for all tested samples from "*D*-only" parameterization method and contour maps illustrating *D* as a function of sample composition (PDF)

■ AUTHOR INFORMATION

Corresponding Author

William F. Schneider − *Department of Chemical and Biomolecular Engineering, University of Notre Dame, Notre Dame, Indiana 46556, United States;* orcid.org/0000-0003-0664-2138; Email: wschneider@nd.edu

Authors

Anshuman Goswami − *Department of Chemical and Biomolecular Engineering, University of Notre Dame, Notre Dame, Indiana 46556, United States*

Siddarth H. Krishna − *Charles D. Davidson School of Chemical Engineering, Purdue University, West Lafayette, Indiana 47907, United States;* orcid.org/0000-0001-5742-7388

Rajamani Gounder − *Charles D. Davidson School of Chemical Engineering, Purdue University, West Lafayette, Indiana 47907, United States;* orcid.org/0000-0003-1347-534X

Complete contact information is available at: https://pubs.acs.org/10.1021/acscatal.4c01856

Notes

The authors declare no competing financial interest.

■ ACKNOWLEDGMENTS

We acknowledge the financial support provided by the National Science Foundation DMREF program under award number 1922173-CBET. The computing resources and technical support for this work were provided by the Notre Dame Center for Research Computing. We also thank Prof. Alex Dowling (University of Notre Dame) for helpful technical discussions.

■ REFERENCES

(1) Bull, I.; Boorse, R. S.; Jaglowski, W. M.; Kormer, G. S.; Moini, A.; Patchett, J. A.; Xue, W.-M.; Burk, P.; Dettling, J. C.; Caudle, M. T. Copper CHA Zeolite Catalysts. U.S. Patent 20,080,226,545 A1, 2008.

(2) Kwak, J. H.; Tonkyn, R. G.; Kim, D. H.; Szanyi, J.; Peden, C. H. Excellent activity and selectivity of Cu− SSZ− 13 in the selective catalytic reduction of NOx with NH_3. *J. Catal.* **2010**, *275*, 187−190.

(3) Peden, C. H. Cu/Chabazite catalysts for 'Lean-Burn' vehicle emission control. *J. Catal.* **2019**, *373*, 384−389.

(4) Paolucci, C.; Di Iorio, J.; Ribeiro, F.; Gounder, R.; Schneider, W. Catalysis science of NO_x selective catalytic reduction with ammonia over Cu-SSZ-13 and Cu-SAPO-34. *Adv. Catal.* **2016**, *59*, 1−107.

(5) Paolucci, C.; Di Iorio, J. R.; Schneider, W. F.; Gounder, R. Solvation and mobilization of copper active sites in zeolites by ammonia: consequences for the catalytic reduction of nitrogen oxides. *Acc. Chem. Res.* **2020**, *53*, 1881−1892.

(6) Hun Kwak, J.; Zhu, H.; Lee, J. H.; Peden, C. H.; Szanyi, J. Two different cationic positions in Cu− SSZ− 13? *Chem. Commun.* **2012**, *48*, 4758−4760.

(7) Giordanino, F.; Vennestrøm, P. N. R.; Lundegaard, L. F.; Stappen, F. N.; Mossin, S.; Beato, P.; Bordiga, S.; Lamberti, C. Characterization of Cu-exchanged SSZ-13: a comparative FTIR, UV-Vis, and EPR study with Cu-ZSM-5 and Cu-β with similar Si/Al and Cu/Al ratios. *Dalton Trans.* **2013**, *42*, 12741−12761.

(8) Borfecchia, E.; Lomachenko, K.; Giordanino, F.; Falsig, H.; Beato, P.; Soldatov, A.; Bordiga, S.; Lamberti, C. Revisiting the nature of Cu sites in the activated Cu− SSZ− 13 catalyst for SCR reaction. *Chem. Sci.* **2015**, *6*, 548−563.

(9) Paolucci, C.; Parekh, A. A.; Khurana, I.; Di Iorio, J. R.; Li, H.; Albarracin Caballero, J. D.; Shih, A. J.; Anggara, T.; Delgass, W. N.; Miller, J. T.; Ribeiro, F. H.; Gounder, R.; Schneider, W. F. Catalysis in a cage: condition-dependent speciation and dynamics of exchanged Cu cations in SSZ− 13 zeolites. *J. Am. Chem. Soc.* **2016**, *138*, 6028−6048.

(10) Paolucci, C.; Khurana, I.; Parekh, A. A.; Li, S.; Shih, A. J.; Li, H.; Di Iorio, J. R.; Albarracin-Caballero, J. D.; Yezerets, A.; Miller, J. T.; Delgass, W. N.; Ribeiro, F. H.; Schneider, W. F.; Gounder, R. Dynamic multinuclear sites formed by mobilized copper ions in NOx selective catalytic reduction. *Science* **2017**, *357*, 898−903.

(11) Lomachenko, K. A.; Borfecchia, E.; Negri, C.; Berlier, G.; Lamberti, C.; Beato, P.; Falsig, H.; Bordiga, S. The Cu− CHA deNOx catalyst in action: temperature-dependent NH_3-assisted selective catalytic reduction monitored by operando XAS and XES. *J. Am. Chem. Soc.* **2016**, *138*, 12025−12028.

(12) Janssens, T. V.; Falsig, H.; Lundegaard, L. F.; Vennestrøm, P. N. R.; Rasmussen, S. B.; Moses, P. G.; Giordanino, F.; Borfecchia, E.; Lomachenko, K. A.; Lamberti, C.; Bordiga, S.; Godiksen, A.; Mossin, S.; Beato, P. A consistent reaction scheme for the selective catalytic reduction of nitrogen oxides with ammonia. *ACS Catal.* **2015**, *5*, 2832−2845.

(13) Gao, F.; Walter, E. D.; Kollar, M.; Wang, Y.; Szanyi, J.; Peden, C. H. Understanding ammonia selective catalytic reduction kinetics over Cu/SSZ− 13 from motion of the Cu ions. *J. Catal.* **2014**, *319*, 1−14.

(14) Gao, F.; Washton, N. M.; Wang, Y.; Kollár, M.; Szanyi, J.; Peden, C. H. Effects of Si/Al ratio on Cu/SSZ− 13 NH_3-SCR catalysts: Implications for the active Cu species and the roles of Brønsted acidity. *J. Catal.* **2015**, *331*, 25−38.

(15) Gao, F.; Mei, D.; Wang, Y.; Szanyi, J.; Peden, C. H. Selective catalytic reduction over Cu/SSZ− 13: linking homo-and heterogeneous catalysis. *J. Am. Chem. Soc.* **2017**, *139*, 4935−4942.

(16) Jones, C. B.; Khurana, I.; Krishna, S. H.; Shih, A. J.; Delgass, W. N.; Miller, J. T.; Ribeiro, F. H.; Schneider, W. F.; Gounder, R. Effects of dioxygen pressure on rates of NOx selective catalytic reduction with NH_3 on Cu-CHA zeolites. *J. Catal.* **2020**, *389*, 140−149.

(17) Krishna, S. H.; Goswami, A.; Wang, Y.; Jones, C. B.; Dean, D. P.; Miller, J. T.; Schneider, W. F.; Gounder, R. Influence of framework Al density in chabazite zeolites on copper ion mobility and reactivity during NO x selective catalytic reduction with NH3. *Nat. Catal.* **2023**, *6*, 276−285.

(18) DeLuca, M.; Jones, C. B.; Krishna, S. H.; Goswami, A.; Saxena, R.; Li, S.; Prasad, S.; Moini, A.; Schneider, W. F.; Gounder, R. Effects of zeolite framework topology on Cu (I) oxidation and Cu (II) reduction kinetics of NOx selective catalytic reduction with NH3. *Chem Catal.* **2023**, *3*, 100726.

(19) Krishna, S. H.; Jones, C. B.; Gounder, R. Temperature dependence of Cu(I) oxidation and Cu(II) reduction kinetics in the selective catalytic reduction of NOx with NH_3 on Cu-chabazite zeolites. *J. Catal.* **2021**, *404*, 873−882.

(20) Feng, Y.; Wang, X.; Janssens, T. V.; Vennestrøm, P. N. R.; Jansson, J.; Skoglundh, M.; Gronbeck, H. First-principles microkinetic model for low-temperature NH_3-assisted selective catalytic reduction of NO over Cu− CHA. *ACS Catal.* **2021**, *11*, 14395−14407.

(21) Millan, R.; Cnudde, P.; Van Speybroeck, V.; Boronat, M. Mobility and Reactivity of Cu+ Species in Cu− CHA Catalysts under

NH_3-SCR-NOx Reaction Conditions: Insights from AIMD Simulations. *JACS Au* **2021**, *1*, 1778−1787.
(22) Metkar, P. S.; Harold, M. P.; Balakotaiah, V. Experimental and kinetic modeling study of NH_3-SCR of NOx on Fe− ZSM− 5, Cu-chabazite and combined Fe-and Cu-zeolite monolithic catalysts. *Chem. Eng. Sci.* **2013**, *87*, 51−66.
(23) Joshi, S. Y.; Kumar, A.; Luo, J.; Kamasamudram, K.; Currier, N. W.; Yezerets, A. New insights into the mechanism of NH_3-SCR over Cu-and Fe-zeolite catalyst: Apparent negative activation energy at high temperature and catalyst unit design consequences. *Appl. Catal., B* **2018**, *226*, 565−574.
(24) De-La-Torre, U.; Pereda-Ayo, B.; Gutiérrez-Ortiz, M. A.; González-Marcos, J. A.; González-Velasco, J. R. Steady-state NH_3-SCR global model and kinetic parameter estimation for NOx removal in diesel engine exhaust aftertreatment with Cu/chabazite. *Catal. Today* **2017**, *296*, 95−104.
(25) Gong, J.; Narayanaswamy, K.; Rutland, C. J. Heterogeneous ammonia storage model for NH_3−SCR modeling. *Ind. Eng. Chem. Res.* **2016**, *55*, 5874−5884.
(26) Olsson, L.; Wijayanti, K.; Leistner, K.; Kumar, A.; Joshi, S. Y.; Kamasamudram, K.; Currier, N. W.; Yezerets, A. A multi-site kinetic model for NH_3-SCR over Cu/SSZ− 13. *Appl. Catal., B* **2015**, *174*−*175*, 212−224.
(27) Bendrich, M.; Scheuer, A.; Hayes, R.; Votsmeier, M. Unified mechanistic model for Standard SCR, Fast SCR, and NO_2SCR over a copper chabazite catalyst. *Appl. Catal., B* **2018**, *222*, 76−87.
(28) Daya, R.; Trandal, D.; Menon, U.; Deka, D. J.; Partridge, W. P.; Joshi, S. Y. Kinetic Model for the Reduction of Cu(II) Sites by NO +NH_3 and Reoxidation of NH_3-Solvated Cu(I) Sites by O_2 and NO in Cu− SSZ− 13. *ACS Catal.* **2022**, *12*, 6418−6433.
(29) Daya, R.; Deka, D. J.; Goswami, A.; Menon, U.; Trandal, D.; Partridge, W. P.; Joshi, S. Y. A redox model for NO oxidation, NH3 oxidation and high temperature standard SCR over Cu-SSZ-13. *Appl. Catal., B* **2023**, *328*, 122524.
(30) Gillespie, D. T. A general method for numerically simulating the stochastic time evolution of coupled chemical reactions. *J. Comput. Phys.* **1976**, *22*, 403−434.
(31) Gillespie, D. T. Exact stochastic simulation of coupled chemical reactions. *J. Phys. Chem.* **1977**, *81*, 2340−2361.
(32) Goswami, A. Zeolite Monte Carlo. 2022, https://github.com/Anshu2711/zmc/.
(33) Shahriari, B.; Swersky, K.; Wang, Z.; Adams, R. P.; De Freitas, N. Taking the human out of the loop: A review of Bayesian optimization. *Proc. IEEE* **2016**, *104*, 148−175.
(34) Iman, R. L.; Davenport, J. M.; Zeigler, D. K. *Latin Hypercube Sampling (Program User's Guide).[LHC, in FORTRAN]*, 1980.
(35) Daulton, S.; Balandat, M.; Bakshy, E. Differentiable expected hypervolume improvement for parallel multi-objective Bayesian optimization. *Adv. Neural Inf. Process. Syst.* **2020**, *33*, 9851−9864.
(36) Daulton, S.; Balandat, M.; Bakshy, E. Parallel bayesian optimization of multiple noisy objectives with expected hypervolume improvement. *Adv. Neural Inf. Process. Syst.* **2021**, *34*, 2187−2200.
(37) Balandat, M.; Karrer, B.; Jiang, D. R.; Daulton, S.; Letham, B.; Wilson, A. G.; Bakshy, E. BoTorch: A Framework for Efficient Monte-Carlo Bayesian Optimization. *Adv. Neural Inf. Process. Syst.* **2020**, *33*, 21524−21538.
(38) Baerlocher, C. International Zeolite Association. 2022, http://www.iza-online.org/.
(39) Wu, Y.; Ma, Y.; Wang, Y.; Rappé, K. G.; Washton, N. M.; Wang, Y.; Walter, E. D.; Gao, F. Rate Controlling in Low-Temperature Standard NH_3-SCR: Implications from Operando EPR Spectroscopy and Reaction Kinetics. *J. Am. Chem. Soc.* **2022**, *144*, 9734−9746.
(40) Millan, R.; Bello-Jurado, E.; Moliner, M.; Boronat, M.; Gomez-Bombarelli, R. Effect of framework composition and NH3 on the diffusion of Cu+ in Cu-CHA catalysts predicted by machine-learning accelerated molecular dynamics. *ACS Cent. Sci.* **2023**, *9*, 2044−2056.
(41) Stamatakis, M.; Vlachos, D. G. Unraveling the Complexity of Catalytic Reactions via Kinetic Monte Carlo Simulation: Current Status and Frontiers. *ACS Catal.* **2012**, *2*, 2648−2663.
(42) Matera, S.; Schneider, W. F.; Heyden, A.; Savara, A. Progress in Accurate Chemical Kinetic Modeling, Simulations, and Parameter Estimation for Heterogeneous Catalysis. *ACS Catal.* **2019**, *9*, 6624−6647.
(43) Krishna, S. H.; Jones, C. B.; Gounder, R. Dynamic Interconversion of Metal Active Site Ensembles in Zeolite Catalysis. *Annu. Rev. Chem. Biomol. Eng.* **2021**, *12*, 115−136.

https://doi.org/10.1021/acscatal.4c01856
ACS Catal. 2024, 14, 8376−8388